HHS Public Access

Author manuscript

Cancer Res. Author manuscript; available in PMC 2020 July 01.

Published in final edited form as:

Cancer Res. 2020 January 01; 80(1): 69–78. doi:10.1158/0008-5472.CAN-19-1237.

Suppression of LIM Kinase 1 and LIM Kinase 2 Limits Glioblastoma Invasion

Joseph Chen[1,*], **Badriprasad Ananthanarayanan**[1,*], **Kelsey S. Springer**[1], **Kayla J. Wolf**[1,2], **Sharon M. Sheyman**[1], **Vivien D. Tran**[1,2], **Sanjay Kumar**[1,2,3,+]

[1]Department of Bioengineering, University of California, Berkeley, Berkeley, CA

[2]UC Berkeley-UC San Francisco Graduate Program in Bioengineering, Berkeley, CA

[3]Department of Chemical and Biomolecular Engineering, University of California, Berkeley, Berkeley, CA

Abstract

The aggressive brain tumor glioblastoma (GBM) is characterized by rapid cellular infiltration of brain tissue, raising the possibility that disease progression could potentially be slowed by disrupting the machinery of cell migration. The LIM kinase isoforms LIMK1 and LIMK2 (LIMK1/2) play important roles in cell polarization, migration, and invasion and are markedly upregulated in GBM and many other infiltrative cancers. Yet, it remains unclear whether LIMK suppression could serve as a viable basis for combating GBM infiltration. In this study, we investigated effects of LIMK 1/2 suppression on GBM invasion by combining GBM culture models, engineered invasion paradigms, and mouse xenograft models. While knockdown of either LIMK1 or LIMK2 only minimally influenced invasion in culture, simultaneous knockdown of both isoforms strongly reduced the invasive motility of continuous culture models and human GBM tumor-initiating cells (TICs) in both Boyden Chamber and 3D hyaluronic acid spheroid invasion assays. Further, LIMK1/2 functionally regulated cell invasiveness in part by disrupting polarized cell motility under confinement and cell chemotaxis. In an orthotopic xenograft model where TICs stably transduced with LIMK1/2 shRNA were implanted intracranially in immunocompromised mice, tumors derived from LIMK1/2 knockdown TICs were substantially smaller and showed delayed growth kinetics and more distinct margins than tumors derived from control TICs. Overall, LIMK1/2 suppression increased mean survival time by 30%. These findings indicate that LIMK1/2 strongly regulate GBM invasive motility and tumor progression and support further exploration of LIMK1/2 as druggable targets.

Keywords

Glioblastoma; mechanobiology; cell motility; cytoskeleton; LIMK

[+] For correspondence: Department of Bioengineering, University of California, Berkeley, 274A Stanley Hall, Berkeley, CA 94720, P: (510)643-0787, F: (510)642-5835, skumar@berkeley.edu.

[*]These authors contributed equally to this work

The authors declare no potential conflicts of interest

Introduction

The brain tumor glioblastoma (GBM) carries a median survival time of only 12–15 months even with aggressive surgical care, radiotherapy, and chemotherapy (1,2). The rapid and intimate infiltration of tumor cells through the surrounding tissue renders complete surgical resection virtually impossible (3,4) and contributes to resistance to a variety of therapeutic agents, including ionizing radiation and anti-angiogenic drugs (5,6). The aggressive spread of this cancer is complex, involving multiple routes of invasion through the dense neural architecture. GBM cells must dynamically adopt various morphologies to enable effective 1D locomotion, confined migration, and 3D invasion to navigate the GBM microenvironment; however, the mechanisms by which GBM cells modulate their cellular architecture is incompletely understood (7–9). As a result, there is growing interest in dissecting the molecular mechanisms that drive GBM cell invasion with an eye towards identifying novel biomarkers and targets for pharmacological intervention (10).

While cell migration is a complex process involving many molecular components, the coordinated action of the actomyosin cytoskeleton plays a particularly central role in generating the protrusive and contractile forces needed for locomotion (11,12). The Rho-family GTPases (e.g., Rho, Rac, Cdc42) organize the actomyosin cytoskeleton, with Rho driving the assembly and contraction of actomyosin bundles that pull against the extracellular matrix (ECM) and Rac stimulating actin polymerization at the cell front to drive protrusion (13). We previously showed that a balance between RhoA-mediated contraction and Rac1-mediated protrusion governs motility in GBM cells (14). We subsequently showed that constitutive activation of RhoA-dependent myosin contractility sensitizes human GBM tumor initiating cells (TICs) to matrix stiffness cues and dramatically slows invasion *in vivo* (15). Others have shown that Rac1 activity promotes invasion by stimulating protrusive activity that promotes an invasive phenotype (16,17). Although RhoA and Rac1 govern distinct functions of the actomyosin cytoskeleton, each GTPase acts through an effector kinase (ROCK for Rho, PAK for Rac) to phosphorylate a common protein, LIM kinase (LIMK) (18,19). LIMK may then phosphorylate and inactivate the actin-severing protein cofilin, thereby stabilizing actin filaments (20,21). Interestingly, the LIMK isoforms LIMK1 and LIMK2 (LIMK 1/2) have been implicated in cancer cell invasion (22–25). For example, Rac-mediated activation of LIMK1 reorganizes the cytoskeleton to promote the invasion of prostate cancer cells (23). Additionally, overexpression of LIMK1 promotes tumor metastasis in a breast cancer model (22). LIMK1/2 are upregulated in GBM, and small molecule inhibitors of cofilin phosphorylation reduce proliferation, adhesion, and invasion of GBM cell lines *in vitro* (26). Despite these intriguing and promising results, the mechanistic role and *in vivo* significance of LIMK in driving GBM invasion remains incompletely explored.

In this study, we investigate contributions of LIMK 1/2 to GBM progression and invasion using a combination of traditional and engineered invasion paradigms as well as mouse xenograft models. While suppression of either isoform alone minimally impacts migration, tandem suppression of both isoforms functionally reduces GBM invasion both *in vitro* and *in vivo*. Tumors derived from LIMK-suppressed TICs exhibit slower growth kinetics, more circumscribed morphologies, and smaller tumor volumes, leading to significantly extended

survival. Our work demonstrates that LIMK1/2 suppression slows GBM progression by reducing invasive motility and supports further exploration of LIMK inhibition as a strategy for reducing GBM invasion.

Materials and Methods

Continuous cell line culture

U373-MG human GBM cells (hereafter referred to as U373 cells) were obtained from the University of California, Berkeley (Berkeley, CA) Tissue Culture Facility, and cultured as previously described (27). The tumor cells were cultured adherently in DMEM (Life Technologies, 11965118) supplemented with 10% fetal calf serum (J.R. Scientific, 44709), 1% penicillin/streptomycin (Thermo Scientific, 15140–122), MEM nonessential amino acids (Thermo Scientific, 11140–050), and sodium pyruvate (Thermo Scientific, 11360–070). Cells were authenticated via short tandem repeats (STR) analysis, tested for *Mycoplasma* (Agilent, 302107) every three months, and passaged and maintained at 37°C and 5% CO_2 with media changes every three to four days. All experiments were performed within 10 cell passages from the frozen stock.

Patient derived primary cell culture

A patient-specific human brain tumor sample used in this study (L0) was collected in a previous study (28) after written informed consent from male patients who underwent surgical treatment and Institutional Review Board approval. Briefly, cells were propagated in neurosphere assay growth conditions with serum-free media (Neurocult NS-A Proliferation kit, Stem Cell Technologies, 05750, 05753) that contained epidermal growth factor (EGF, 20 ng/mL, R&D Systems, 236-EG-01M), basic fibroblast growth factor (bFGF, 10 ng/mL, R&D Systems, 233-FB-025/CF), and heparin (0.2% diluted in PBS, Sigma-Aldrich, H4784). The tumor cells form gliomaspheres in suspension and were serially passaged every 5 to 7 days via disassociation with Accutase (Innovative Cell Technologies, AT104). For bioluminescence imaging, TICs were transduced with a luciferase reporter. These cells have been transcriptionally characterized and classified as the Classical subtype of GBM (25). STR analysis (University of Arizona Genetics Core; Tucson, AZ) confirmed that these cells had not been contaminated by any known cell lines, and regular *Mycoplasma* testing ensured that cultures were free of *Mycoplasma* contamination.

shRNA Knockdown

To create LIMK1 knockdown cells, at least two distinct shRNAs targeting human LIMK1 were obtained from Sigma-Aldrich in pLKO.1-puro vectors (Sigma-Aldrich, SHC001; sequences in Supplementary Table S1). Lentiviral particles were packaged in HEK 293T cells and purified using standard procedures (29). Bulk populations of U373 and L0 cells were transduced with viral particles at a multiplicity of infection (MOI) ≤ 1, and shRNA-expressing cells were selected using 1 μg/mL puromycin. To create LIMK1/2 double knockdown cells, shRNA oligos targeting human LIMK2 with the appropriate overhangs were annealed and ligated into pLKO.1-hygro (Addgene, 24150) digested with AgeI (NEB, R3552S) and EcoRI (NEB, R3101S). These vectors were similarly packaged into lentiviral particles, and cells transduced with both LIMK1- and LIMK2-targeting viral vectors were

selected with both 1 μg/mL puromycin (Invitrogen, A1113803) and 100 μg/mL hygromycin (Corning, MT30240CR). Knockdown efficiency was assessed by western blot. Vectors containing non-targeting shRNA sequences were used to create control cells that were similarly selected with both antibiotics. TIC shRNA-expressing cells were maintained under full selection media.

Western blotting

GBM cells were washed twice in PBS and lysed with RIPA buffer supplemented with HALT protease and phosphatase inhibitor (Thermo Scientific, 78442), 1% sodium molybdate (Sigma-Aldrich, 737860) and 3% sodium fluoride (Sigma-Aldrich, 215309). Cells were centrifuged to remove membrane components. Protein quantification was conducted via BCA Protein Assay (Pierce, 23225), and samples were normalized with respect to protein content. Proteins were separated via SDS-PAGE and transferred onto a nitrocellulose membrane (Li-Cor, 926–31092). Membranes were blocked in Li-Cor blocking buffer for 1 h and incubated with primary antibody (rabbit LIMK1 (1:1000, Cell Signaling 3842S); rabbit LIMK2 (1:1000, Cell Signaling 3845S); rabbit pCofilin (1:1000, Cell Signaling 3313S); rabbit Cofilin (1:1000, Cell Signaling 5175S); and GAPDH (1:5000, Sigma-Aldrich G8795)) overnight at 4°C. Membranes were then washed 3X in TBST and incubated for 1 h with Li-Cor near IR secondary antibodies (1:10000, anti-mouse 800, 925–32210 and anti-rabbit 680, 92–68071) followed by 3 TBST washes and imaged via Odyssey CLx (Li-Cor).

Boyden Chamber (Transwell) Invasion Assay

Transwell inserts of 8 and 3 μm pore sizes (Corning, 3422) were functionalized with 100 μg/ml laminin (Invitrogen, 23017–015) for 3 h at 37 °C and then seeded in the upper chamber with 8000 cells per insert in basal medium. The bottom chamber was filled with basal media supplemented with 20 ng/ml EGF (R&D Systems, 236-EG-01M) as a chemoattractant. Cells were allowed to migrate for 24 h and were then fixed with 4% PFA for 15 mins and washed 3X with PBS. Wells were then stained with propidium iodide (Cell Signaling, 4087S) overnight and imaged with a Nikon TE200E2 microscope. Cell counting was analyzed with ImageJ (National Institutes of Health).

Hyaluronic Acid (HA)-RGD Invasion Assay

HA hydrogels were fabricated as previously described (30). Briefly, HA-methacrylate (Me-HA) was synthesized by treating sodium hyaluronate (Lifecore Biomedical, Research Grade, 66 kDa–99 kDa, HA60K) with methacrylic anhydride (Sigma-Aldrich, 94%, 276685). The extent of methacrylation per disaccharide was quantified by ^{1}H NMR as detailed previously and found to be ~85% for materials used in this study. RGD peptide Ac-GCGYGRGDSPG-NH2 (Anaspec, AS-62349) was added at a concentration of 0.5 mmol/L to provide integrin-binding functionality. Gels were crosslinked with an MMP degradable peptide (KKCGGPQGIWGQGCKK, Genscript, 0.68 mmol/L) (31) in phenol-free DMEM (Invitrogen, 21063–029) to facilitate cell matrix degradation and invasion. 1.5 wt/wt% HA-RGD gels with a shear modulus of ~300 Pa were generated to study 3D spheroid invasion of U373 cells. The shear moduli of hydrogel formulations were measured using oscillatory rheometry (Anton Parr Physica MCR 310) as described previously (30). Briefly, hydrogels were first crosslinked by incubation for 1 h in a humidified 37°C chamber. Rheological

testing consisted of frequency sweeps ranging from 100 to 0.1 Hz at 0.5% amplitude also in a humidified 37°C chamber. The reported shear modulus is the average storage modulus for 3 tests per type of matrix composition at an oscillation frequency of 0.5 Hz. Tumor spheroids were created using the hanging drop method as previously described (32). Briefly, U373 cells were suspended in growth media and 13 μl droplets of cell suspensions containing 500 cells were plated on the lid of a 4 well plate and inverted over wells filled with PBS. After 5 days, spheres were collected and mixed in with HA-RGD and crosslinker to initiate gelation. 5 μl of gel solution was then pipetted onto a hydrophobic dish and allowed to crosslink. Medium was added after 1 hour and spheres were monitored over 14 days. Invasion data is presented as a relative change in spheroid area from day 1 to day 14.

Microchannel Fabrication

Silicon masters were fabricated using established lithography techniques as previously described (33). Briefly, wafers were cleaned with a piranha solution (3:1 sulfuric acid to hydrogen peroxide), rinsed with water, and baked to remove residual water. The wafers were then spin-coated with SU-8 2010 (Microchem) and photopatterned with the microchannel designs (Supplemental Figure 1). Next, the wafers were given a post-exposure bake followed by a hard bake. Finally, the wafer was treated with dimethyldichloromethylsilane (Sigma-Aldrich, 440248) to prevent the PDMS from sticking to the wafer. Sylgard 184 base and curing agent (Krayden Inc, DC4019862) were mixed in a 10:1 ratio, degassed, and then poured onto the wafer to a thickness of ~ 2 mm. The PDMS devices were placed at 80°C for 2 h to cure. After curing, the devices were cut out with a razor blade and adhered to tissue culture polystyrene dishes with sterile vacuum grease to allow for cell seeding and time-lapse microscopy.

Cell Protrusion Quantification

KymographClear and KymographDirect were utilized for quantitative assessment of protrusion dynamics as previously described (34). LifeAct U373 NT and LIMK1/2 KD cells were imaged every 5 min for 3 h, and stacks were registered using StackReg via ImageJ. Kymographs were generated using *KymographClear* by using the segmented line tool through the center of the cells, starting from the trailing edge to the leading edge. Kymographs were manually traced and inputted into *KymographDirect* for quantitative analysis. Velocity vs time plots were generated to describe protrusion dynamics and then integrated to determine net protusion displacement. A positive velocity represents protrusion growth in the direction of the leading edge, and a negative velocity represents movment in the direction opposite of the leading edge.

Chemotaxis Assay

U373 cells were seeded into the narrow (1000 × 2000 × 70 μm) channel of a tissue culture treated μ-slide chemotaxis chamber (Ibidi, 80326). After an overnight incubation, the chemotaxis chamber was filled with DMEM containing 20 ng/ml EGF (R&D Systems, 236-EG-01M). The observation area within the channel was imaged by phase-contrast microscopy via a 10X objective. Images were captured every 10 min for 16 h, and cell migration tracks between 4 and 16 h were analyzed with ImageJ using a manual tracking plugin and with the Chemotaxis and Migration Tool (Ibidi).

Immunostaining and Structured Illumination Microscopy (SIM)

For SIM imaging, cells were plated on laminin coated #0 coverslip dishes (MatTek, P35G-0–20-C). Cells were fixed and permeabilized with a 1 min incubation in 0.3% glutaraldehyde, 0.25% Triton-X 100 solution in cytoskeletal buffer (10 mM MES monohydrate, 150 mM NaCl, 5 mM EGTA, 5 mM glucose, and 5 mM $MgCl_2$; pH 6.1) followed by a 20 min incubation in 3% glutaraldehyde solution in cytoskeletal buffer. Cells were then reduced with two 5 min incubations with 0.1% $NaBH_4$ and washed three times in PBS. The cells were then blocked with 5% goat serum in PBS for 1 h and subsequently stained with Phallodin 546 (1:500; Invitrogen, A22283) overnight at 4°C. After staining, the cells were given three 10 min washes and then directly imaged using a Zeiss Elyra structured illumination microscope and a Plan-Apochromat 63X/1.4 Oil DIC M27 objective (Zeiss). Samples were illuminated using an Argon multiline laser for excitation at 546 nm diode laser. Samples were captured with z-stack slices of 1 μm and SIM processed via Zen 2010 software. Using ImageJ, captured cells were presented as maximum intensity 3D projections.

Mouse Xenograft Model

Female 6-month old non-obese diabetic/severe combined immunodeficient gamma (NSG) mice (NOD.Cg-Prkdc(scid)Il2rg(tm1Wjl)/ SzJ) (Jackson Laboratory) were implanted intracranially with 150,000 NT or LIMK1/2 L0 TICs following institutional and national regulations, and according to a previously established protocol (28). Briefly, animals were anesthetized using 3.5% isoflurane and then maintained at 2% isoflurane for the duration of the surgery. The animals were secured onto a stereotactic apparatus, and a dental Dremel drill with a 0.5 mm bit was used to create a single hole 2 mm lateral right from the bregma. 3 μl of cell solution was added at a rate of 1 μl/min using a 26 gauge needle at a depth of 3 mm. After surgery, the animals were rested on a heating pad and treated with analgesics 0.1 mg/kg buprenorphine and 5 mg/kg meloxicam. Additionally, the mice were treated daily with a single dose of 10 mg/kg meloxicam and two doses of 0.05 mg/kg buprenorphine for 6 days. A total of fifteen mice were used for each cohort, and five from each group were sacrificed at a set 6 week time point to properly compare tumor size between NT and LIMK1/2 KD groups. The remaining ten animals from each cohort were followed until humane limits were reached. All procedures were conducted under protocols approved by the Institutional Animal Care and Use Committee at UC Berkeley.

Histological Analysis

Tissue processing and immunohistochemistry were performed on free-floating sections following previously published techniques (35). Briefly, mice were anaesthetized with 100 mg/kg ketamine-xylazine (Sigma-Aldrich, K113) and transcardially perfused with 0.9% saline. Brains were removed and fixed in 4% paraformaldehyde, at 4 °C for 48 h and then incubated in a 30% sucrose for cryoprotection. After the brains sunk down in the sucrose solution, they were sectioned coronally at 40 μm with a cryomicrotome (Leica) and each section was stored in cryoprotective medium. For staining, brain sections were mounted onto frosted microscope slides and blocked with 5% goat serum in PBS for 1 h. Then, tissue sections were stained with mouse anti-Nestin (1:200; EMD Millipore MAB5326), rabbit

anti-Ki-67 (1:200; Cell Signaling 9129S), and DAPI (1:500; Thermo Scientific D1306) overnight at 4°C. Next, the tissue was washed 3X and incubated with fluorophore-conjugated secondary antibodies for 1 h at room temperature and subsequently mounted with Fluoromount Aqueous Mounting Media (Sigma-Aldrich F4680).

For histological staining, standard procedures were used to dehydrate the tissue and stain with hematoxylin and eosin (Sigma-Aldrich HHS16, E4009) to identify tumors. Low magnification images were taken with the Zeiss Axio Scan.Z1 and higher magnification images were taken with a Nikon TE200E2 microscope.

Statistical Analysis

The data are reported as the mean of all replicates, and error bars are given as standard error of the mean. GraphPad Prism 7 software was used to created figures, and statistical significance between sample groups were determined by one-way ANOVA and Holm-Sidek tests unless otherwise noted. Details of comparisons and replicates are provided in the appropriate figure legend.

Results

Upregulation of LIMK1/2 in GBM is associated with high grade and poor prognosis

A key premise of our study is that targeting LIMK, a central regulator of actin-based motility, may prove effective in limiting GBM infiltration. As a first step towards assessing the clinical significance of this premise, we queried The Cancer Genome Atlas (TCGA) to determine whether transcriptomic and clinical features of GBM might be associated with changes in expression of LIMK and a set of other candidate proteins relevant to actin-based cell motility. Frequently mutated genes (*EGFR, CDKN2A, PTEN, PDGFRA*) were used as controls to ensure that proper statistical thresholds (e.g., z-scores) were used for the analysis of the TCGA dataset. We found that within this list of actin related genes, *LIMK1* was among the most altered loci, with ~ 21% of patients exhibiting increases in DNA copy number and/or mRNA levels. Genes that make up the Apr2/3 complex (*ARPC1A, ARPC1B, and WASL*) were similarly altered in GBM patients as was Rac1. Further, modifications of *LIMK2* were observed in ~ 5% of patients (Figure 1A). We then explored changes in mRNA levels between GBM and low-grade gliomas (which are generally much less invasive) to identify actin-related genes that may be enriched in the high-grade cohort. We found that within this candidate list of actin-based cell motility genes, *LIMK1* mRNA levels ranked second-highest, indicating a strong association between LIMK1 and disease severity (Figure 1B). Further, Kaplan-Meier analysis showed significantly decreased survival in patients with increases in LIMK1 and LIMK2 (Figure 1C).

Combined knockdown of LIMK1/2 disrupts actin polymerization and dynamics

Given the strong clinical association between GBM progression and LIMK expression, we hypothesized that suppression of LIMK might attenuate the invasive phenotype. We therefore used shRNAs to suppress expression of LIMK proteins in culture, beginning with U373 human GBM cells. Surprisingly, although we were successfully able to individually knock down either LIMK1 or LIMK2 nearly completely without changes in total levels of

the other isoform, neither knockdown produced significant reductions in cofilin phosphorylation. However, combined knockdown of LIMK1/2 together produced a dramatic reduction in cofilin phosphorylation, indicating increased cofilin activity (Figure 2A). These data suggest that LIMK1/2 play overlapping roles in the regulation of cofilin, and that loss of both isoforms is necessary for cofilin disinhibtion. To confirm that LIMK1/2 suppression is associated with reductions in polymerized actin, we applied SIM to image actin cytoskeletal architecture. As expected, we did not observe changes in cell morphology or cytoskeletal organization in NT and single knockdown lines, whereas in the double knockdown lines, we observed a near-absence of actin filaments and bundles within the cell interior (Figure 2B). To gain insight into effects on actin dynamics, we transduced our control and double KD cells with LifeAct and used time lapse imaging to capture actin cycling. We observed classic actin retrograde flow within the lamellipodia of the NT lines (kymographs); however, LIMK1/2 KD lines showed random actin cycling with no clear actin structures, revealing significant alterations in actin structure, organization, and dynamics (Figure 2C; Supplemental Video 1). Further analysis revealed a loss of cell polarization in the KD lines and a significant decrease in net protrusion displacement (Figure 2D,E). Velocity vs time plots of cell protrusions were generated via *KymographDirect* and showed dramatically different protrusive character in NT and LIMK1/2 KD lines. NT cells exhibited stable protrusion growth velocities in the leading edge with an expected reduction in velocity over time as the lamellipodia matured. Similarly, the trailing edge velocity was relatively stable over time. However, LIMK1/2 KD cell protrusions in both directions were highly variable with positive and negative velocities, indicating rapid protrusion extension and retraction with an inability to mature (Figure 2F–G). Together, these data show that suppression of LIMK1/2 reduces cofilin phosphorylation, thereby promoting actin cleavage and disassembly, which disrupts protrusive growth, dynamics, and ultimately polarization. Because suppression of both isoforms is needed to influence cofilin phosphorylation, we focused on LIMK1/2 KD cells in all subsequent studies.

LIMK1/2 knockdown decreases cell invasiveness

We next examined the functional consequence of LIMK1/2 knockdown on cell invasion by conducting 2D motility, Boyden Chamber, and 3D spheroid invasion assays. 2D motility showed no differences (Supplemental Figure 2A,B), but Boyden Chamber studies revealed that LIMK1/2 KD cell lines have significantly reduced cell invasion through both 8 and 3 μm diameter pores, with this reduction becoming more pronounced with decreased pore size (Figure 3A). Thus, suppression of LIMK 1/2 renders cells less capable of tightly confined invasion, an important mode of invasion necessary for spread throughout the brain parenchyma (36). To verify this finding in a completely independent paradigm, we conducted 3D spheroid invasion assays in protease-degradable hydrogels composed of hyaluronic acid (HA, the primary brain ECM component), a 3D culture model we had previously shown recapitulates invasive morphologies seen in brain tissue (30) (Figure 3B). Indeed, LIMK1/2 KD cells were significantly impaired in their ability to invade through HA, confirming that LIMK1/2 suppression functionally reduces cell invasion within confined, 3D environments.

LIMK1/2 knockdown dysregulates confined migration and chemotaxis

Our Boyden Chamber and 3D spheroid studies indicate that LIMK1/2 KD strongly suppresses invasion. However, these paradigms interrogate the combined effect of multiple cellular processes, including chemotaxis and confined migration. To gain deeper mechanistic insight into the origin of these results, we examined the effect of LIMK1/2 KD on 1D confined migration and chemotaxis using microchannels. In addition to being compatible with live-cell imaging, both chemotaxis and migration through confined spaces are important features of GBM invasion *in vivo* (37,38). In previous studies, we have found microchannel-based scaffolds serve as a useful surrogate for contact guidance-medated invasion reminiscent of that observed along vascular beds and white matter tracts (33,39–42). We fabricated PDMS devices with varying width channels ranging from 5 – 100 μm and measured migration speed along the channels. As anticipated, when NT cells were fully confined by both walls in the 5 μm-wide channels, these cells migrated faster than in fully unconfined matrices, which we and others have previously observed and attributed to the enforced polarization (43). More importantly, LIMK1/2 KD cells migrated significantly slower than NT cells specifically when confined by 5 μm wide channels, which points to the particular significance of LIMK1/2 mediated polarization dynamics in the mode of migration most relevant to GBM invasion *in vivo*. This reduction in migration speed was not observed in single-KD cell lines (Supplemental Figure 3). LIMK1/2 KD cells exhibited a disorganized actin cytoskeletal architecture and were incapable of polarizing and forming actin cables necessary for efficient cell motility on 1D (Figure 4A) (44). We then investigated the ability of the KD cells to respond to chemotactic cues, motivated by the reported roles of cofilin in shaping directional migration (45–47). Under an EGF gradient, ~75% of NT cells fell within the upper quadrants of a Wind-Rose plot, demonstrating a strong chemotactic effect as expected. Conversely, under the same stimulus, LIMK1/2 KD cells migrated much more randomly as evidenced by the even distribution of cells within migration paths in all quadrants (Figure 4B). Further, the LIMK1/2 KD cells not only showed aberrant chemotaxis but also exhibited slower overall migration speeds (Figure 4C). Thus, suppression of LIMK1/2 slows cell invasion by limiting cell polarization and rapid migration along 1D confined channels as well as by disrupting chemotaxis.

Knockdown of LIMK1/2 decreases TIC invasiveness

While the above results strongly support the idea that LIMK 1/2 suppression limits invasion, the use of U373 cells carries important caveats. Continous GBM culture models are widely acknowledged to suffer from significant genetic drift, which may result in part from chronic conditioning to highly aphysiological culture conditions (48). Moreover, continuous culture models frequently form circumscribed tumors *in vivo* as opposed to the more infiltrative lesions characteristic of GBM (49). To extend our findings to a more clinically proximal culture model, we turned to a classical-subtype human GBM tumor-initiating cell (TIC) line (L0) that forms infiltrative tumors in mouse xenograft studies (15,28). We began by knocking down LIMK1 and 2 using our shRNA constructs and confirming knockdown via western blotting (Figure 5A). We observed comparable cytoskeletal alterations and reduced cofilin phosphorylation to LIMK1/2 KD U373 cells (Figure 5A,B). For example, control TICs assembled F-actin bundles along the cell perimeter, whereas these structures were not visible in LIMK1/2 KD TICs. Importantly, when we conducted Boyden Chamber assays

with 8 and 3 μm pore sizes, we saw a U373-like reduction in cell invasiveness in the knockdown cells, which was also enhanced with smaller pore sizes (Figure 5C,D). Overall, the phenotypes we observed upon LIMK suppression in U373 cells were broadly reproduced in TICs.

LIMK1/2 knockdown reduces tumor growth and invasion and extends survival in vivo

As described above, a key advantage of TICs is that they more closely recapitulate defining pathological features of GBM when orthtopically xenografted into immunocompromised mice. To test whether LIMK1/2 knockdown could influence tumor progression *in vivo*, we injected NT and LIMK1/2 KD TICs intracranially into separate cohorts of NSG mice (n = 15). For each cohort, we sacrificed 5 animals at 6 weeks post-implantation to enable direct comparison between NT and LIMK1/2 KD tumors and then followed tumor evolution until animal death for the rest of the group. In order to quantify tumor growth kinetics, TICs were transduced with a luciferase reporter and monitored longitudinally with bioluminescence imagng. Strikingly, we observed robust decreases in bioluminescence signal in the LIMK1/2 KD cohort, suggesting that the tumors were much smaller and spread at dramatically slower rates (Figure 6A–C). Further, animal survival was prolonged by ~30% in the LIMK1/2 KD animals (Figure 6D). Quantification of tumor volume from histological analysis at 6 weeks supported the bioluminescence data and revealed a strong reduction in tumor occupancy in the LIMK1/2 KD groups (Figure 6E,F). Moreover, endpoint immunohistochemistry (IHC) showed that although LIMK1/2 KD tumors continued to spread, the tumor margins were more distinct with less diffuse invasion into the parenchyma, as evidenced by the lack of nestin-positive TICs outside the tumor mass (Figure 6G). IHC also showed comparable levels of Ki-67 positive cells, ruling out dramatic changes in proliferation rates between the two groups. Staining for LIMK1/2 in tumor sections revealed enriched LIMK1/2 within the tumor mass in NT groups and confirmed loss of LIMK1/2 in the KD animals (Supplemental Figure 4). Collectively, and consistent with our culture studies, these data indicate that suppression of LIMK 1/2 drastically impedes tumor growth and spread *in vivo* by disrupting invasion.

Discussion

Aggressive cell infiltration is a hallmark of GBM, and there is a significant need to better understand the biophysical mechanisms of invasion and leverage these insights for diagnosis, prognosis, and therapy (3,4,10,50). While work from our own laboratory and many others has strongly implicated Rho and Rac GTPase-driven cytoskeletal remodeling as a critical driver of invasion (11,12), it has remained unclear how suppression of effectors common to both pathways might influence invasion. Here, we investigate one such common effector, LIMK, which is activated by the Rho effector ROCK and the Rac effector PAK1 to promote actin polymerization. We combine traditional and engineered culture paradigms to show that simultaneous suppression of both isoforms LIMK1 and LIMK2 reduces invasion through disrupted cell polarization, impaired chemotaxis, and ability to navigate confined spaces. Moreover, suppression of LIMK1/2 *in vivo* produces more circumscribed and less infiltrative tumors, resulting in a ~30% extension in survival. These findings strongly show

that disrupting cell invasion effectively abrogates GBM progression and support further preclinical exploration of LIMK1/2 inhibition as a strategy for limiting GBM invasion.

Modulation of LIMK1/2 can regulate cell motility *in vitro* by regulating cofilin activity (22–25,51,52). However, comparatively little is known about the extent to which these effects translate to mechanisms of motility relevant to GBM *in vivo* invasion, which may be markedly different from standard 2D motility (43). In GBM, cells invade either slowly through the brain parenchyma and/or rapidly along white matter tracts and vascular beds, which contribute to diffuse infiltration and seeding of secondary tumors (3,37,53). Migration along white matter tracts and blood vessels may be regarded as a sort of 1D motility in which polarity is enforced by association with a linear structure. Although loss of LIMK 1/2 does not appreciably change rates of random 2D motility in unconfined environments, significant alterations were seen in cell polarization, protrusion displacement, and protrusion dynamics. The inability of LIMK1/2 KD cells to polarize and generate stable protrusions led to motility deficits that were exposed in 1D microchannels. Notably, confined 1D motility is dependent on formin based actin assembly mechanisms, which rely heavily on the assembly and contraction of actin cables, which were not observed in the LIMK1/2 KD cells (44). This disruption of actin architecture and decreases in 1D motility was not observed in single KD lines, showing that knockdown of both isoforms is necessary to alter the canonical regulation of actin assembly and disassembly via cofilin (Supplemental Figure 3). Interestingly, differences between NT and LIMK1/2 knockdown cell migration were minimized as channel width increased and cells began to adopt a 2D based motility (Supplemental Figure 2A,B). These findings are consistent with at least one previous report in which LIMK1/2 inhibition was observed to minimally influence 2D motility (54). Together these findings indicate that LIMK1/2 affects 1D polarized migration to a much greater extent than random 2D motility, which may explain the pronounced effect on GBM tumor infiltration *in vivo*. Our finding that LIMK 1/2 suppression also impairs chemotactic migration suggests a general role for these proteins in supporting polarized motility and is consistent with previous work implicating cofilin activity in the establishment of polarity (45,46).

While we primarily interpret our results in terms of actin assembly, LIMK is also an established regulator of microtubule organization (55,56), implying that its suppression may influence mitotic spindle positioning and proliferation (57). Inhibition of LIMK has been observed to affect microtubule organization and slow mitosis, motivating exploration of LIMK as a chemotherapeutic target (55). Interestingly, LIMK2 has been reported to play an important microtubule-dependent role in chemoresistance, with inhibition of LIMK2 restoring chemosensitivity (58). Although we did not observe strongly LIMK-dependent changes in proliferation *in vivo*, it will be important in future studies to clarify the role of LIMK-dependent microtubule behavior in tumor progression *in vivo*.

Finally, our *in vivo* experiments with primary TICs support further exploration of pharmacological inhibition of LIMK1/2 in GBM therapeutics. We show that targeting the TIC population leads to reduced tumor size and clearer tumor margins in a mouse model, providing evidence that attenuating invasive motility is sufficient to significantly improve survival. It will be fruitful to revisit these studies with a wide diversity of GBMs to

determine whether sensitivity to LIMK suppression is a universal feature or instead varies in some systematic way, such as by molecular subtype. Although orthotopic xenograft models have their disadvantages such as the absence of an adaptive immune system and potential variabilities in tumor initiation and engraftment, this system does allow one to follow the progression of human tumor cells *in vivo*. Nonetheless, it would be important to examine functional contributions in LIMK1/2 in other mouse models, including genetically engineered mouse models. These models would also be ideal settings in which to test small-molecule LIMK inhibitors, which would be expected to target both LIMK isoforms. Several small molecule inhibitors of LIMK have been described with a range of efficacy in many *in vitro* studies across different types of cancers (14,59–61). Indeed, early studies of the LIMK inhibitors BMS-5 and Cucurbitacin with continuous GBM lines have shown promise with respect to reducing adhesion and invasion, with comparatively little cytotoxicity to normal astrocytes (26). Current efforts to develop effective compounds have significantly optimized binding affinity and pharmacokinetic parameters such as bioavailability, half-life, and clearance (62). Given this progress, we anticipate that it will be fruitful to more fully characterize mechanisms through which LIMK1/2, its effectors, and its regulators mechanistically contribute to GBM invasion.

Supplementary Material

Refer to Web version on PubMed Central for supplementary material.

Acknowledgements

Axio Scan images were taken at the CRL Molecular Imaging Center at UC Berkeley supported by National Science Foundation Grant No. DBI-1041078. The authors would like to acknowledge Holly Aaron and Feather Ives for their assistance and training. Structured illumination microscopy was conducted at the UC Berkeley Biological Imaging Facility, which is supported by the National Instititues of Health S10 program under Award No 1S10(D018136-01). The authors would like to thank Dr. Steve Ruzin and Dr. Denise Schichnez for their assistance and training. The authors gratefully acknowledge financial support from the following sources: National Institues of Health (Ruth L. Kirschstein Postdoctoral Individual National Research Award No. F32CA221366 to J.C., F31CA228317 to K.J.W., R01GM122375 and R01CA227136 to S.K.), National Science Foundation (Graduate Research Fellowship Program to V.D.T.), and the W.M. Keck Foundation (S.K).

References

1. Rulseh AM, Keller J, Klener J, Sroubek J, Dbalý V, Syrůček M, et al. Long-term survival of patients suffering from glioblastoma multiforme treated with tumor-treating fields. World J Surg Oncol. 2012;10:220. [PubMed: 23095807]
2. Omuro A, DeAngelis LM. Glioblastoma and other malignant gliomas: a clinical review. JAMA. 2013;310:1842–50. [PubMed: 24193082]
3. Davis ME. Glioblastoma: Overview of Disease and Treatment. Clin J Oncol Nurs. 2016;20:1–14.
4. Lieberman F Glioblastoma update: molecular biology, diagnosis, treatment, response assessment, and translational clinical trials. F1000Research. 2017;6:1892. [PubMed: 29263783]
5. Pàez-Ribes M, Allen E, Hudock J, Takeda T, Okuyama H, Viñals F, et al. Antiangiogenic Therapy Elicits Malignant Progression of Tumors to Increased Local Invasion and Distant Metastasis. Cancer Cell. 2009;15:220–31. [PubMed: 19249680]
6. Jahangiri A, Nguyen A, Chandra A, Sidorov MK, Yagnik G, Rick J, et al. Cross-activating c-Met/β1 integrin complex drives metastasis and invasive resistance in cancer. Proc Natl Acad Sci U S A. National Academy of Sciences; 2017;114:E8685–94.
7. Wolf KJ, Chen J, Coombes JD, Aghi MK, Kumar S. Dissecting and rebuilding the glioblastoma microenvironment with engineered materials. Nat Rev Mater. Nature Publishing Group; 2019;1–18.

8. De Gooijer MC, Navarro MG, Bernards R, Wurdinger T, Van Tellingen O. An Experimenter's Guide to Glioblastoma Invasion Pathways. 2018;
9. Chen J, Kumar S. Biophysical regulation of cancer stem/initiating cells: Implications for disease mechanisms and translation. Curr Opin Biomed Eng. Elsevier; 2017;1:87–95.
10. Nakada M, Nakada S, Demuth T, Tran NL, Hoelzinger DB, Berens ME. Molecular targets of glioma invasion. Cell Mol Life Sci. 2007;64:458–78. [PubMed: 17260089]
11. Yamaguchi H, Condeelis J. Regulation of the actin cytoskeleton in cancer cell migration and invasion. Biochim Biophys Acta - Mol Cell Res. 2007;1773:642–52.
12. Yilmaz M, Christofori G. EMT, the cytoskeleton, and cancer cell invasion. Cancer Metastasis Rev. 2009;28:15–33. [PubMed: 19169796]
13. Maekawa M Signaling from Rho to the Actin Cytoskeleton Through Protein Kinases ROCK and LIM-kinase. Science (80-). 1999;285:895–8.
14. Mackay JL, Kumar S. Simultaneous and independent tuning of RhoA and Rac1 activity with orthogonally inducible promoters. Integr Biol (United Kingdom). Royal Society of Chemistry; 2014;6:885–94.
15. Wong SY, Ulrich TA, Deleyrolle LP, MacKay JL, Lin J-MG, Martuscello RT, et al. Constitutive activation of myosin-dependent contractility sensitizes glioma tumor-initiating cells to mechanical inputs and reduces tissue invasion. Cancer Res. NIH Public Access; 2015;75:1113–22.
16. Teng TS, Lin B, Manser E, Ng DCH, Cao X. Stat3 promotes directional cell migration by regulating Rac1 activity via its activator PIX. J Cell Sci. 2009;122:4150–9. [PubMed: 19861492]
17. Chen H-Y, Shen C-H, Tsai Y-T, Lin F-C, Huang Y-P, Chen R-H. Brk activates rac1 and promotes cell migration and invasion by phosphorylating paxillin. Mol Cell Biol. American Society for Microbiology Journals; 2004;24:10558–72.
18. Foletta VC, Moussi N, Sarmiere PD, Bamburg JR, Bernard O. LIM kinase 1, a key regulator of actin dynamics, is widely expressed in embryonic and adult tissues. Exp Cell Res. 2004;294:392–405. [PubMed: 15023529]
19. Acevedo K, Moussi N, Li R, Soo P, Bernard O. LIM kinase 2 is widely expressed in all tissues. J Histochem Cytochem. 2006;54:487–501. [PubMed: 16399995]
20. Cuberos H, Vallée B, Vourc HP, Tastet J, Andres CR, Bénédetti H. Roles of LIM kinases in central nervous system function and dysfunction. FEBS Lett. Federation of European Biochemical Societies; 2015;589:3795–806.
21. Prunier C, Prudent R, Kapur R, Sadoul K, Lafanechère L. LIM kinases: cofilin and beyond. Oncotarget. 2017;8:41749–63. [PubMed: 28445157]
22. Bagheri-Yarmand R, Mazumdar A, Sahin AA, Kumar R. LIM kinase 1 increases tumor metastasis of human breast cancer cells via regulation of the urokinase-type plasminogen activator system. Int J Cancer. 2006;118:2703–10. [PubMed: 16381000]
23. Davila M, Frost AR, Grizzle WE, Chakrabarti R. LIM kinase 1 is essential for the invasive growth of prostate epithelial cells: Implications in prostate cancer. J Biol Chem. 2003;278:36868–75. [PubMed: 12821664]
24. Liao Q, Li R, Zhou R, Pan Z, Xu L, Ding Y, et al. LIM kinase 1 interacts with myosin-9 and alpha-actinin-4 and promotes colorectal cancer progression. Br J Cancer. Nature Publishing Group; 2017;117:563–71.
25. Su J, Zhou Y, Pan Z, Shi L, Yang J, Liao A, et al. Downregulation of LIMK1-ADF/cofilin by DADS inhibits the migration and invasion of colon cancer. Sci Rep. 2017;7:1–12. [PubMed: 28127051]
26. Park J-B, Agnihotri S, Golbourn B, Bertrand KC, Luck A, Sabha N, et al. Transcriptional profiling of GBM invasion genes identifies effective inhibitors of the LIM kinase-Cofilin pathway. Oncotarget. 2014;5:9382–95. [PubMed: 25237832]
27. Ulrich TA, de Juan Pardo EM, Kumar S. The Mechanical Rigidity of the Extracellular Matrix Regulates the Structure, Motility, and Proliferation of Glioma Cells. Cancer Res. 2009;69:4167–74. [PubMed: 19435897]
28. Deleyrolle LP, Harding A, Cato K, Siebzehnrubl FA, Rahman M, Azari H, et al. Evidence for label-retaining tumour-initiating cells in human glioblastoma. Brain. Oxford University Press; 2011;134:1331–43.

29. Peltier J, Schaffer D V. Viral Packaging and Transduction of Adult Hippocampal Neural Progenitors. Methods Mol Biol. 2010 page 103–16.
30. Ananthanarayanan B, Kim Y, Kumar S. Elucidating the mechanobiology of malignant brain tumors using a brain matrix-mimetic hyaluronic acid hydrogel platform. Biomaterials. NIH Public Access; 2011;32:7913–23.
31. Singh SP, Schwartz MP, Lee JY, Fairbanks BD, Anseth KS. A peptide functionalized poly(ethylene glycol) (PEG) hydrogel for investigating the influence of biochemical and biophysical matrix properties on tumor cell migration. Biomater Sci. 2014;2:1024–34. [PubMed: 25105013]
32. Ulrich TA, Jain A, Tanner K, MacKay JL, Kumar S. Probing cellular mechanobiology in three-dimensional culture with collagen–agarose matrices. Biomaterials. Elsevier; 2010;31:1875–84.
33. Lin J-MG, Kang C-C, Zhou Y, Huang H, Herr AE, Kumar S. Linking invasive motility to protein expression in single tumor cells. Lab Chip. The Royal Society of Chemistry; 2018;18:371–84.
34. Mangeol P, Prevo B, Peterman EJG. *KymographClear* and *KymographDirect* : two tools for the automated quantitative analysis of molecular and cellular dynamics using kymographs. Holzbaur E, editor. Mol Biol Cell. 2016;27:1948–57. [PubMed: 27099372]
35. Villeda SA, Luo J, Mosher KI, Zou B, Britschgi M, Bieri G, et al. The ageing systemic milieu negatively regulates neurogenesis and cognitive function. Nature. NIH Public Access; 2011;477:90–4.
36. Beadle C, Assanah MC, Monzo P, Vallee R, Rosenfeld SS, Canoll P. The Role of Myosin II in Glioma Invasion of the Brain. Holzbaur E, editor. Mol Biol Cell. 2008;19:3357–68. [PubMed: 18495866]
37. Wolf KJ, Lee S, Kumar S. A 3D topographical model of parenchymal infiltration and perivascular invasion in glioblastoma. Cit APL Bioeng. 2018;2:31903.
38. de Gooijer MC, Guillén Navarro M, Bernards R, Wurdinger T, van Tellingen O. An Experimenter's Guide to Glioblastoma Invasion Pathways. Trends Mol Med. Elsevier Current Trends; 2018;24:763–80.
39. Pathak A, Kumar S. Independent regulation of tumor cell migration by matrix stiffness and confinement. Proc Natl Acad Sci U S A. National Academy of Sciences; 2012;109:10334–9.
40. Gallego-Perez D, Higuita-Castro N, Denning L, DeJesus J, Dahl K, Sarkar A, et al. Microfabricated mimics of in vivo structural cues for the study of guided tumor cell migration. Lab Chip. The Royal Society of Chemistry; 2012;12:4424.
41. Cha J, Koh I, Choi Y, Lee J, Choi C, Kim P. Tapered Microtract Array Platform for Antimigratory Drug Screening of Human Glioblastoma Multiforme. Adv Healthc Mater. John Wiley & Sons, Ltd; 2015;4:405–11.
42. Beliveau A, Thomas G, Gong J, Wen Q, Jain A. Aligned Nanotopography Promotes a Migratory State in Glioblastoma Multiforme Tumor Cells. Sci Rep. Nature Publishing Group; 2016;6:26143.
43. Doyle AD, Wang FW, Matsumoto K, Yamada KM. One-dimensional topography underlies three-dimensional fibrillar cell migration. J Cell Biol. Rockefeller University Press; 2009;184:481–90.
44. Monzo P, Chong YK, Guetta-Terrier C, Krishnasamy A, Sathe SR, Yim EKF, et al. Mechanical confinement triggers glioma linear migration dependent on formin FHOD3. Mol Biol Cell. 2016;27:1246–61. [PubMed: 26912794]
45. Nishita M, Tomizawa C, Yamamoto M, Horita Y, Ohashi K, Mizuno K. Spatial and temporal regulation of cofilin activity by LIM kinase and Slingshot is critical for directional cell migration. J Cell Biol. 2005;171:349–59. [PubMed: 16230460]
46. Mouneimne G, DesMarais V, Sidani M, Scemes E, Wang W, Song X, et al. Spatial and Temporal Control of Cofilin Activity Is Required for Directional Sensing during Chemotaxis. Curr Biol. Cell Press; 2006;16:2193–205.
47. Wang W, Mouneimne G, Sidani M, Wyckoff J, Chen X, Makris A, et al. The activity status of cofilin is directly related to invasion, intravasation, and metastasis of mammary tumors. J Cell Biol. Rockefeller University Press; 2006;173:395–404.
48. Torsvik A, Stieber D, Enger PØ, Golebiewska A, Molven A, Svendsen A, et al. U-251 revisited: genetic drift and phenotypic consequences of long-term cultures of glioblastoma cells. Cancer Med. John Wiley & Sons, Ltd; 2014;3:812–24.

49. Lee J, Kotliarova S, Kotliarov Y, Li A, Su Q, Donin NM, et al. Tumor stem cells derived from glioblastomas cultured in bFGF and EGF more closely mirror the phenotype and genotype of primary tumors than do serum-cultured cell lines. Cancer Cell. Cell Press; 2006;9:391–403.
50. Khan IS, Ehtesham M. Targeting glioblastoma cancer stem cells: the next great hope? Neurosurg Focus. 2014;37:E7.
51. Nishimura Y, Yoshioka K, Bernard O, Bereczky B, Itoh K. A role of LIM kinase 1/cofilin pathway in regulating endocytic trafficking of EGF receptor in human breast cancer cells. Histochem Cell Biol. 2006;126:627–38. [PubMed: 16763828]
52. Vardouli L, Moustakas A, Stournaras C. LIM-kinase 2 and cofilin phosphorylation mediate actin cytoskeleton reorganization induced by transforming growth factor-β. J Biol Chem. 2005;280:11448–57. [PubMed: 15647284]
53. Yao X The Role of Chemoattractant Receptors in the Progression of Glioma.
54. Scott RW, Hooper S, Crighton D, Li A, König I, Munro J, et al. LIM kinases are required for invasive path generation by tumor and tumor-associated stromal cells. J Cell Biol. Rockefeller University Press; 2010;191:169–85.
55. Mardilovich K, Baugh M, Crighton D, Kowalczyk D, Gabrielsen M, Munro J, et al. LIM kinase inhibitors disrupt mitotic microtubule organization and impair tumor cell proliferation. Oncotarget. 2015;6.
56. Prudent R, Vassal-Stermann E, Nguyen CH, Pillet C, Martinez A, Prunier C, et al. Pharmacological inhibition of LIM kinase stabilizes microtubules and inhibits neoplastic growth. Cancer Res. 2012;72:4429–39. [PubMed: 22761334]
57. Pease JC, Tirnauer JS. Mitotic spindle misorientation in cancer - out of alignment and into the fire. J Cell Sci. 2011;124:1007–16. [PubMed: 21402874]
58. Po'Uha ST, Shum MSY, Goebel A, Bernard O, Kavallaris M. LIM-kinase 2, a regulator of actin dynamics, is involved in mitotic spindle integrity and sensitivity to microtubule-destabilizing drugs. Oncogene. 2010;29:597–607. [PubMed: 19881550]
59. Yin Y, Zheng K, Eid N, Howard S, Jeong J-H, Yi F, et al. Bis-aryl Urea Derivatives as Potent and Selective LIM Kinase (Limk) Inhibitors. J Med Chem. American Chemical Society; 2015;58:1846–61.
60. Farkash EM, Rak R, Elad-Sfadia G, Haklai R, Carmeli S, Kloog Y, et al. Computer-Based Identification of a Novel LIMK1/2 Inhibitor that Synergizes with Salirasib to Destabilize the Actin Cytoskeleton. Oncotarget. Impact Journals; 2012;3:629–39.
61. Goodwin NC, Cianchetta G, Burgoon HA, Healy J, Mabon R, Strobel ED, et al. Discovery of a Type III Inhibitor of LIM Kinase 2 That Binds in a DFG-Out Conformation. ACS Med Chem Lett. American Chemical Society; 2015;6:53–7.
62. Manetti F Recent advances in the rational design and development of LIM kinase inhibitors are not enough to enter clinical trials. Eur J Med Chem. 2018;155:445–58. [PubMed: 29908439]
63. Brennan CW, Verhaak RGW, McKenna A, Campos B, Noushmehr H, Salama SR, et al. The Somatic Genomic Landscape of Glioblastoma. Cell. 2013;155:462–77. [PubMed: 24120142]
64. Gao J, Aksoy BA, Dogrusoz U, Dresdner G, Gross B, Sumer SO, et al. Integrative Analysis of Complex Cancer Genomics and Clinical Profiles Using the cBioPortal. Sci Signal. 2013;6:pl1–pl1. [PubMed: 23550210]
65. Cerami E, Gao J, Dogrusoz U, Gross BE, Sumer SO, Aksoy BA, et al. The cBio Cancer Genomics Portal: An Open Platform for Exploring Multidimensional Cancer Genomics Data: Figure 1. Cancer Discov. 2012;2:401–4. [PubMed: 22588877]

Significance

Targeting the actin-binding proteins LIMK1 and LIMK2 significantly diminishes glioblastoma invasion and spread, suggesting the potential value of these proteins as therapeutic targets.

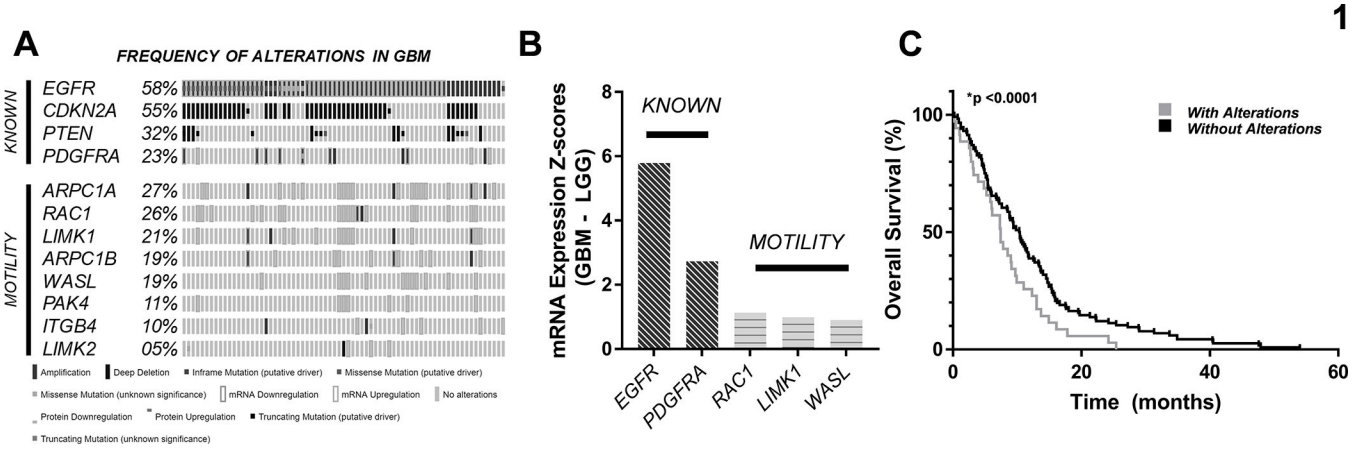

Figure 1. LIMK1/2 expression status is associated with GBM grade and poor prognosis.

The Cancer Genome Atlas (TCGA) was queried using a list of candidate genes involved in actin-based cell motility for alterations observed in GBM tumors, and a z-score threshold of ± 2.0 was set as the statistical threshold. LIMK1 is altered in > 20 % of patients (alterations include amplification of DNA copy number and mRNA upregulation) and is elevated in high grade gliomas when compared to low grade glioma (LGG) groups (**A,B**). Frequently mutated genes (EGFR, CDKN2A, PTEN, TP53) were used as controls to ensure proper statistical thresholds were used in the analysis of the datasets. Kaplan-Meier survival curves show reduced survival time in patients with LIMK alterations (**C**). TCGA Cell 2013 dataset was analyzed via cBioPortal (63–65).

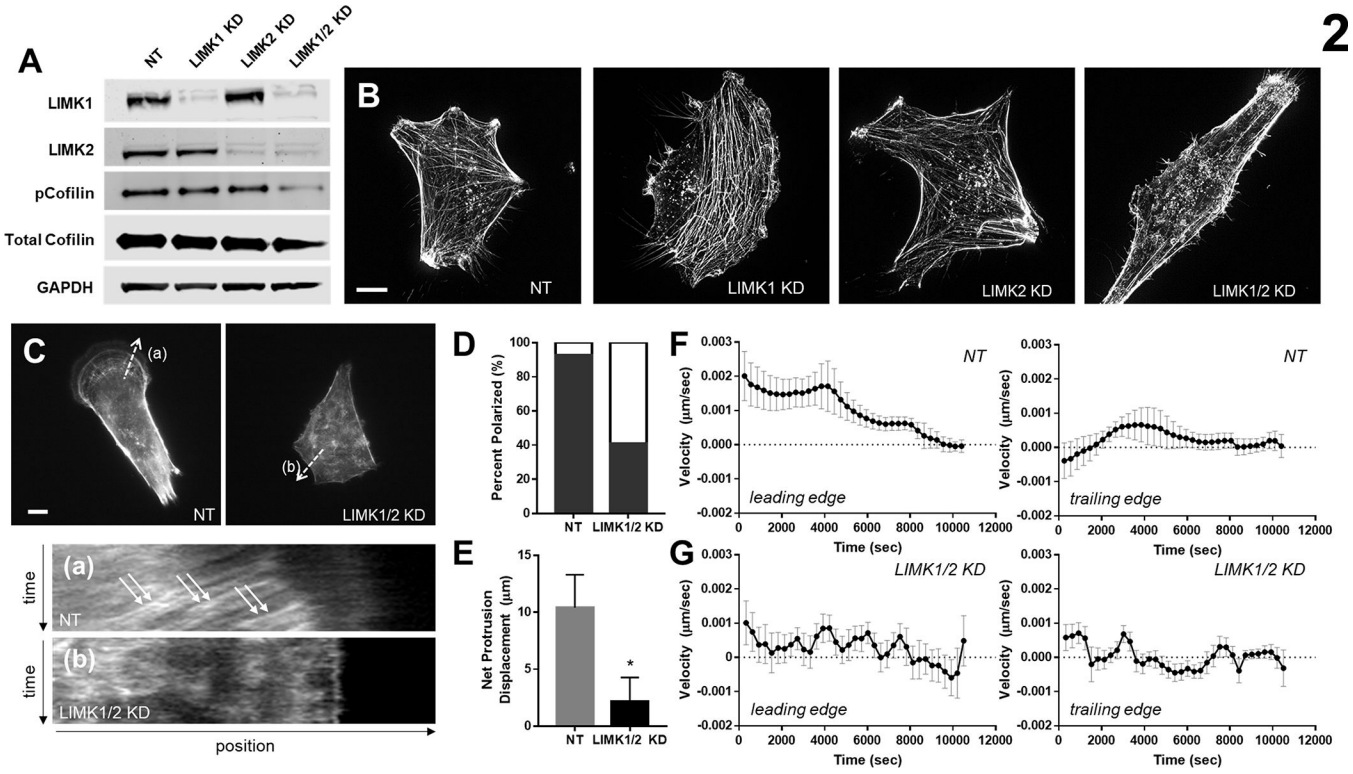

Figure 2. Knockdown of LIMK1/2 disrupts actin polymerization and dynamics.

Single and double LIMK knockdown lines were generated with U373s and investigated for changes in cofilin activity and actin cytoskeletal organization. Single and double knockdown was confirmed via western blot, and cofilin phosphorylation was strongly reduced only in the double knockdown lines (**A**). SIM imaging reveals stable cytoskeletal structure and organization in NT and single knockdown lines but disrupted actin networks in the LIMK1/2 KD lines, providing support for increased cofilin activity (**B**). Further, retrograde flow of actin was clearly seen in NT lines as indicated by the kymograph at the lamellopodia (a); however, the kymograph for LIMK1/2 cells (b) showed abberant actin dynamics and organization (**C**). Quantification of cell polarization and protrusion displacement showed that LIMK1/2 KD cells were unable to display a polarized morphology and generate stable growth in protrusions (**D,E**). Further, quantification of protrusion velocities revealed steady protrusion growth in the NT cells but highly variable protrusion dynamics with frequent changes in direction, indicating constant extension and retraction events in the LIMK1/2 KD cells (**F,G**). * $p < 0.05$, scalebar = 10 μm.

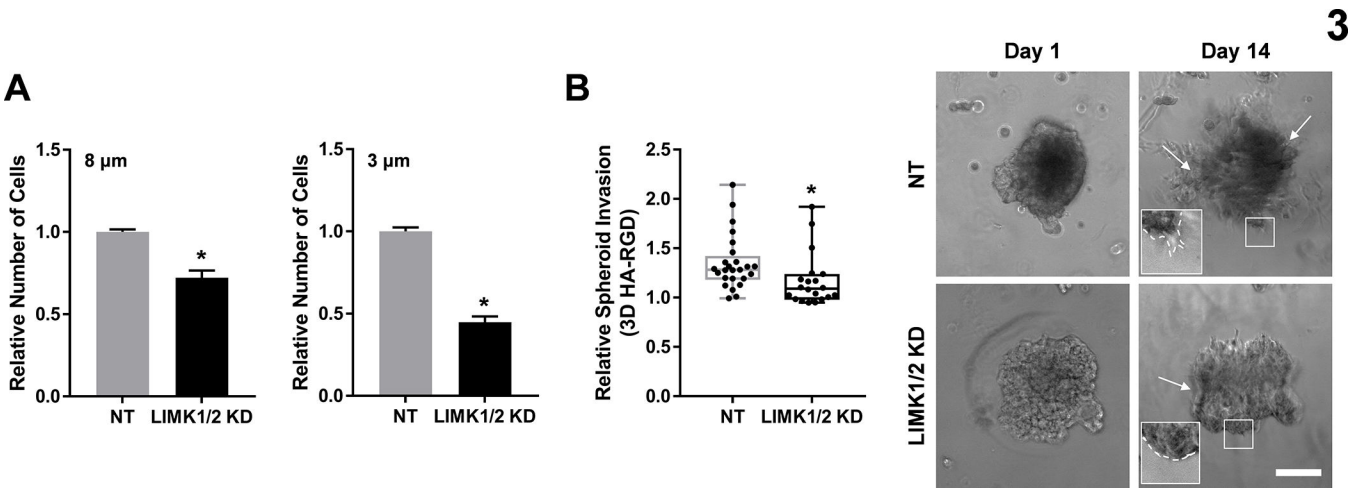

Figure 3. LIMK1/2 knockdown reduces cell invasiveness in vitro.

Boyden chamber assays reveal a significant reduction in cell invasion in both 8 and 3 μm pore sizes with a more dramatic relative change in the 3 μm group (**A**). Similarly, U373 3D spheroid invasion in HA-RGD gels is robustly reduced in LIMK1/2 KD cells (**B**). Representative images show clear protrusions at the sphere periphery in NT groups and clearer edges in the knockdown cells. * $p < 0.05$, scalebar = 100 μm.

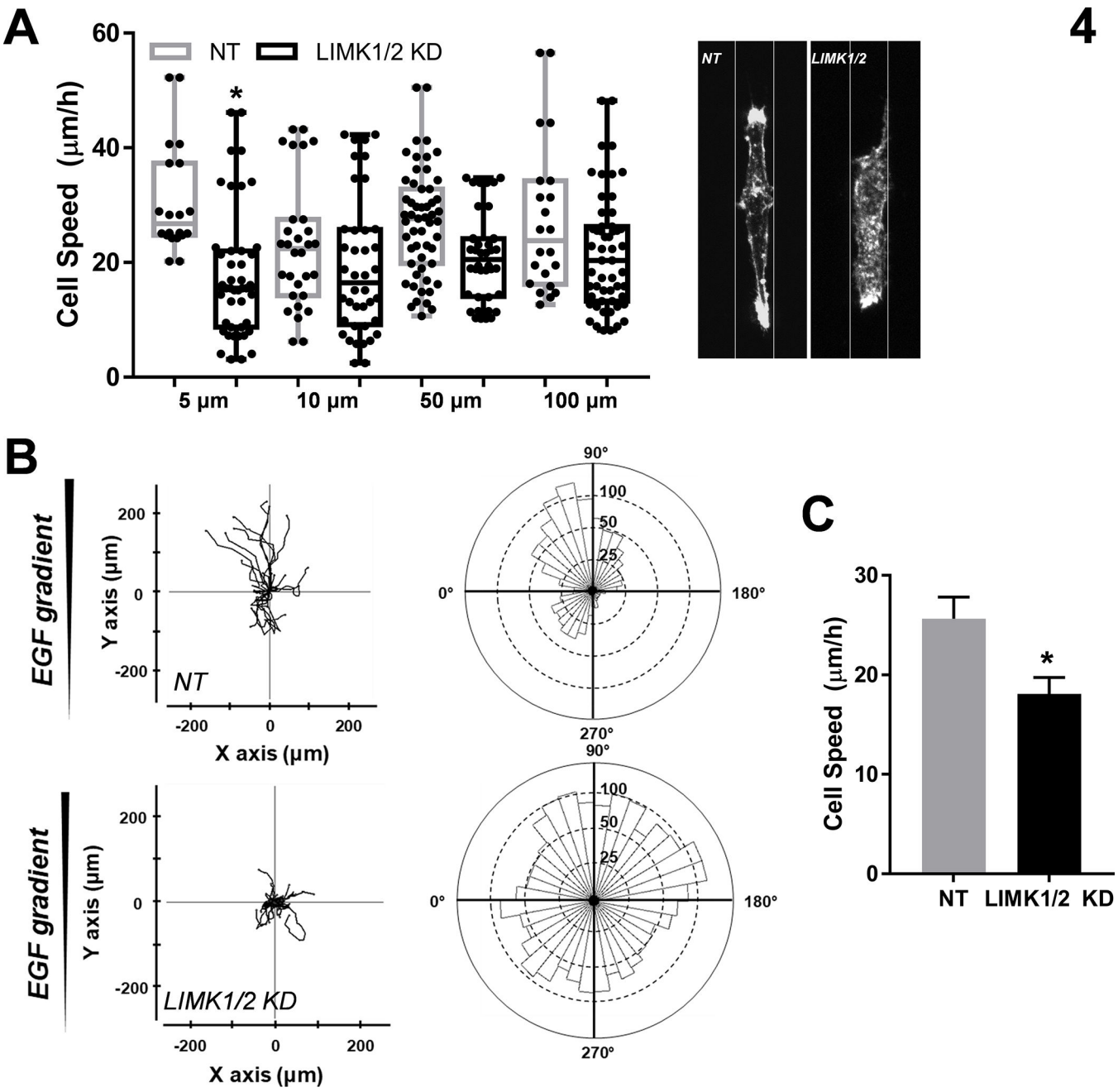

Figure 4. LIMK1/2 knockdown disrupts 1D confined migration and chemotaxis.

Significant differences in confined 1D motility were observed in 5 μm channels with NT cells migrating more quickly than LIMK1/2 KD cells (**A**). The reduced migratory capacity of LIMK1/2 KD cells is associated with actin cytoskeletal disorganization. Further, LIMK1/2 KD cells exhibit robust defects in chemotaxis with a lack of directional persistence under EGF stimulation as well as reduced migration speed (**B,C**). * $p < 0.05$.

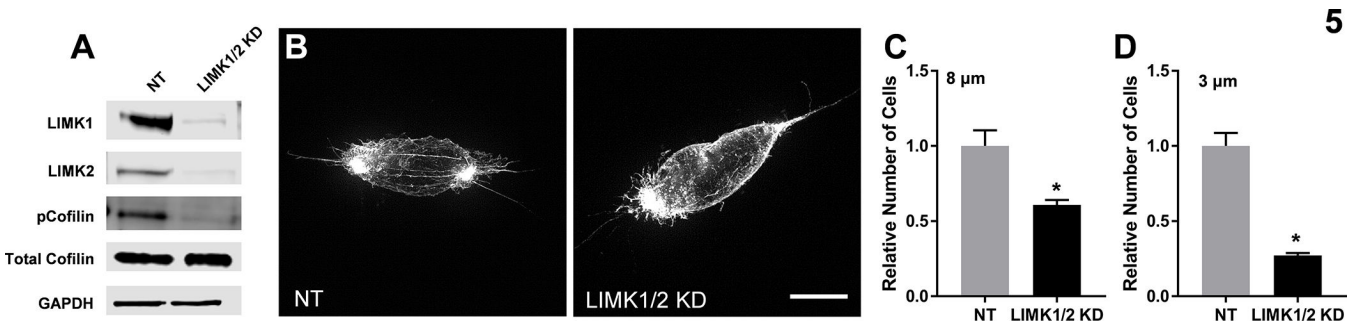

Figure 5. Knockdown of LIMK1/2 decreases TIC invasiveness.

LIMK1/2 was suppressed in TICs as revealed via western blotting. Similar to the U373s, cofilin activity was significantly affected in the double knockdowns (**A**). Further, loss of cytoskeletal organization was also observed via SIM imaging, similar to observations in U373s (**B**). Boyden chamber assays reveal a significant reduction in cell invasiveness in LIMK1/2 KD TICs loaded in 8 μm (**C**) and 3 μm (**D**) pore sizes. 3 μm pore sizes similarly generated a more pronounced relative decrease in invasion as observed in the U373s. * $p < 0.05$, scalebar = 10 μm.

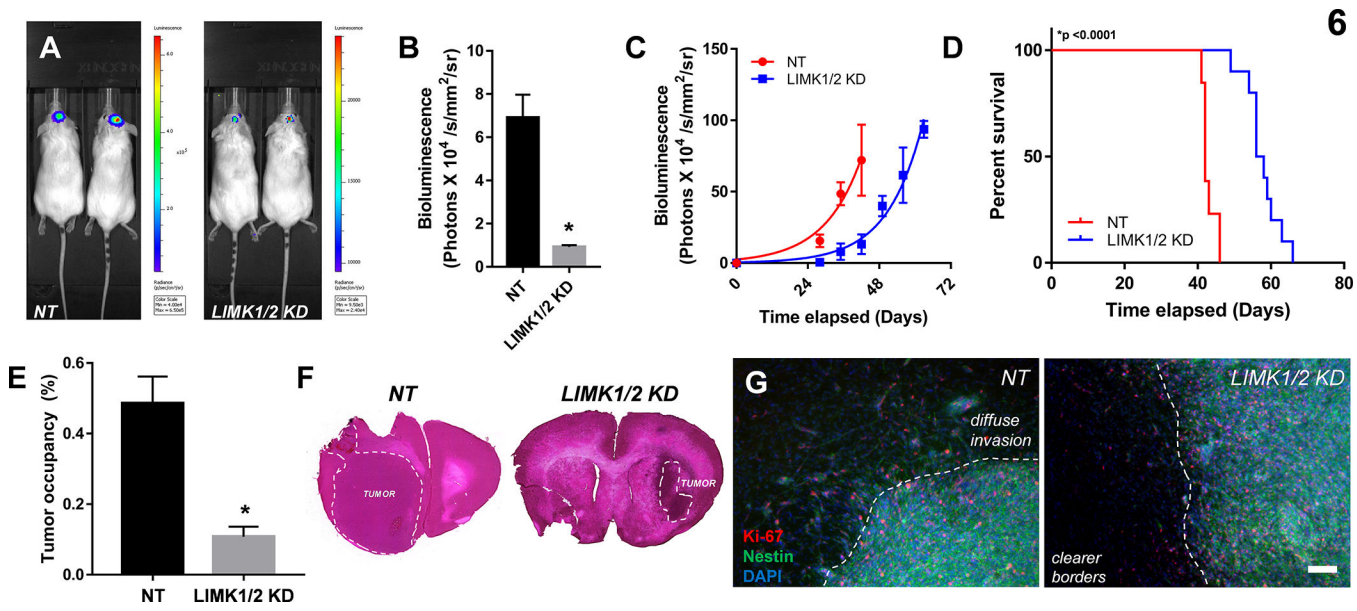

Figure 6. LIMK1/2 knockdown reduces tumor growth and extends survival time in an orthotopic xenograft mouse model.

Animals implanted with LIMK1/2 KD cells generated tumors with reduced bioluminescence signal (day 42) (**A,B**) and delayed tumor kinetics (**C**). This change in tumor progression resulted in a significant ~30% increase in survival time (**D**). Tumor volume was reduced in the LIMK1/2 KD cohort as revealed by H&E staining (**E,F**), and LIMK1/2 KD tumors displayed clearer tumor borders as evidenced by nestin staining at the tumor margins. Further, Ki-67 staining show that tumor proliferation was not significantly affected (**G**). Collectively, these data support a role for LIMK1/2 in regulating cellular invasion and tumor spread. Statistical significance of Kaplan Meier analysis determined by Log-rank (Mantel-Cox) test, * $p < 0.001$, scalebar = 200 μm.